



Integrated Brain Connectivity Analysis with fMRI, DTI, and sMRI Powered by Interpretable Graph Neural Networks

Gang Qu^a, Ziyu Zhou^b, Vince D. Calhoun^c, Aiying Zhang^d, Yu-Ping Wang^{a,*}

^aBiomedical Engineering Department, Tulane University, New Orleans, LA 70118, USA

^bComputer Science Department, Tulane University, New Orleans, LA 70118, USA

^cTri-Institutional Center for Translational Research in Neuro Imaging and Data Science (TreNDS) - Georgia State, Georgia Tech and Emory, Atlanta, GA 30303, USA.

^dSchool of Data Science, University of Virginia, Charlottesville, VA 22903, USA

ARTICLE INFO

Article history:

Keywords: Multimodal Neuroimaging Integration, Cognitive Neuroscience, Functional MRI (fMRI), Diffusion Tensor Imaging (DTI), Structural MRI (sMRI), Graph deep learning, Brain Connectivity, Cognitive Development, Human Connectome Project

ABSTRACT

Multimodal neuroimaging modeling has become a widely used approach but confronts considerable challenges due to heterogeneity, which encompasses variability in data types, scales, and formats across modalities. This variability necessitates the deployment of advanced computational methods to integrate and interpret these diverse datasets within a cohesive analytical framework. In our research, we amalgamate functional magnetic resonance imaging (fMRI), diffusion tensor imaging (DTI), and structural MRI (sMRI) into a cohesive framework. This integration capitalizes on the unique strengths of each modality and their inherent interconnections, aiming for a comprehensive understanding of the brain's connectivity and anatomical characteristics. Utilizing the Glasser atlas for parcellation, we integrate imaging-derived features from various modalities—functional connectivity from fMRI, structural connectivity from DTI, and anatomical features from sMRI—within consistent regions. Our approach incorporates a masking strategy to differentially weight neural connections, thereby facilitating a holistic amalgamation of multimodal imaging data. This technique enhances interpretability at connectivity level, transcending traditional analyses centered on singular regional attributes. The model is applied to the Human Connectome Project's Development study to elucidate the associations between multimodal imaging and cognitive functions throughout youth. The analysis demonstrates improved predictive accuracy and uncovers crucial anatomical features and essential neural connections, deepening our understanding of brain structure and function. This study not only advances multimodal neuroimaging analytics by offering a novel method for the integrated analysis of diverse imaging modalities but also improves the understanding of intricate relationship between the brain's structural and functional networks and cognitive development.

© 2024 Elsevier B. V. All rights reserved.

1. Introduction

Advancements in multimodal neuroimaging have revolutionized our understanding of the human brain by providing a har-

monized view of its structural and functional information (Yan et al., 2022). This comprehensive approach enables simultaneous analysis of the brain's anatomy, connectivity, and activity, deepening our understanding of brain function and cognition by capturing a wider range of brain activity and interactions. Additionally, such integrative investigations are vital for explor-

*Corresponding author: Email: wyp@tulane.edu

ing the intricacies of learning, memory, language, and emotional regulation, and are instrumental in identifying patterns (Qu *et al.*, 2021b; Wang *et al.*, 2024) and deviations across developmental stages that relate to cognitive processes (Uludağ and Roebroeck, 2014; Qu *et al.*, 2020; Sui *et al.*, 2011). At the heart of multimodal neuroimaging are functional magnetic resonance imaging (fMRI) (Glover, 2011; Wang *et al.*, 2021), diffusion tensor imaging (DTI) (O’Donnell and Westin, 2011), and structural magnetic resonance imaging (sMRI) (Symms *et al.*, 2004). By combining these modalities, researchers leverage the strengths and mitigate the weaknesses inherent to each modality (Sui *et al.*, 2014). For instance, fMRI provides insights into brain activity and functional networks (Orlichenko *et al.*, 2022a; Tang *et al.*, 2023) by mapping regions active during cognitive tasks. However, its reliance on hemodynamic responses as proxies, combined with limited temporal resolution, restricts its efficacy in capturing instantaneous neuronal dynamics and providing insights into the physical pathways of the brain. Structural connectivity (SC) from DTI (Finger *et al.*, 2016; Tang *et al.*, 2024) maps the brain’s stable anatomical networks but can be compromised by the complex organization of fibers and susceptibility to imaging artifacts. In contrast, sMRI yields detailed morphological insights (Rykhlevskaia *et al.*, 2008). However, its capacity to uncover the dynamic interactions of functional brain networks remains limited.

Our study stands at the forefront of research efforts that aim to integrate fMRI, sMRI, and DTI modalities. This simultaneous examination is not only essential but also presents substantial methodological challenges. The integration of these modalities is complicated by the high-dimensional nature of neuroimaging data, disparate spatial and temporal resolutions, and data heterogeneity—the variability in data types, scales, and formats. This complexity requires sophisticated methods to preserve the intricate topology of neural networks and ensure that the combined modalities accurately reflect both the structural and functional aspects of the brain. Recent literature has underscored the superiority of integrating multimodal neuroimaging data over the utilization of single modality data in the detection of pathological brain anomalies (Sui *et al.*, 2013; Zhu *et al.*, 2014; Stämpfli *et al.*, 2008) and the prediction of phenotypes (Qu *et al.*, 2021b) by leveraging the complementary strengths of various imaging modalities (Xiao *et al.*, 2022; Wang *et al.*, 2024). For instance, Zhuang *et al.* (Zhuang *et al.*, 2019) investigate extracting unique features from each modality to build predictive models. However, this strategy may not fully encapsulate the complex, interrelated dynamics and synergies that exist between the modalities, potentially limiting the comprehensiveness of the predictive analysis. Moreover, there has been a shift towards adopting purely data-driven methodologies (Zhu *et al.*, 2022; Shi *et al.*, 2020; Hu *et al.*, 2021; Qu *et al.*, 2021a; Patel *et al.*, 2024), incorporating advanced computational models to enhance predictive performance. While these approaches have shown promise in terms of accuracy, they frequently overlook the incorporation of established neuroimaging knowledge (Wang *et al.*, 2023; Zhou *et al.*, 2024; Li *et al.*, 2021), thus treating neuroimaging data comparably to natural images without recognizing the unique characteristics

and requirements of neuroscientific data analysis. This oversight could lead to the underutilization of critical neuroscientific principles that could otherwise inform and refine the modeling process. A significant academic discourse also revolves around the challenge of model interpretation within this context (Hofmann *et al.*, 2022; Orlichenko *et al.*, 2022b). Many contemporary models engage in the extraction of high-level features, which, due to their complexity, become opaque and challenging for human interpretation. Even when post-hoc interpretative techniques are applied to elucidate the workings of these models, the resulting explanations often deviate significantly from neuroscientifically relevant insights. This divergence underscores a critical gap in aligning machine learning interpretability with meaningful neuroscientific inquiry, highlighting the need for methodological advancements that bridge this divide.

To address those challenges, we employ a masked Graph Neural Networks (MaskGNN) framework designed to amalgamate SC, FC, and anatomical statistics (AS) using a unified anatomical atlas (Glasser *et al.*, 2016). This approach aims to standardize heterogeneous data to a common scale and structure it within a universal graph, facilitating a comprehensive analysis across different dimensions of brain connectivity and morphology. These graphs are subsequently integrated through a masked graph neural network (Qu *et al.*, 2021b), which generates a weighted mask to quantify the significance of each edge in the graph, effectively measuring the comprehensive connectivity strength among brain regions. Our methodology stands out in its adaptability across diverse multimodal datasets, employing a flexible strategy for parcellating and integrating data, thereby consolidating diverse connectivity measures into a consolidated schema. This approach enables profound insights into both functional and structural connectivities, ensuring the preservation of network topology for rigorous brain analysis and providing intrinsic interpretability. Our model is validated on the Human Connectome Project in Development (HCP-D) dataset (Somerville *et al.*, 2018) to cognitive score prediction task. The findings reveal that our model outperforms established benchmarks, indicating a notable advancement in the domain of multimodal brain network analysis. Our model is then employed to discern critical brain connections and anatomical biomarkers, elucidating which morphological features are essential for human cognition. These results are corroborated by prior research and yield new and interesting discoveries, reaffirming the advantages of our approach and its potential for further investigation.

Our primary contributions lie in the inherent interpretability of an integrated graph deep learning framework that synthesizes fMRI, sMRI, and DTI. Notably, it introduces: (a) a versatile framework that merges these modalities into coherent graphs while separately delineating FC-SC relationships, setting a foundation for future advanced modeling; (b) a comprehensive system that inherently supports interpretability with additional post-hoc explanations; (c) new insights into the relationship between brain measurements and cognitive development in adolescents.

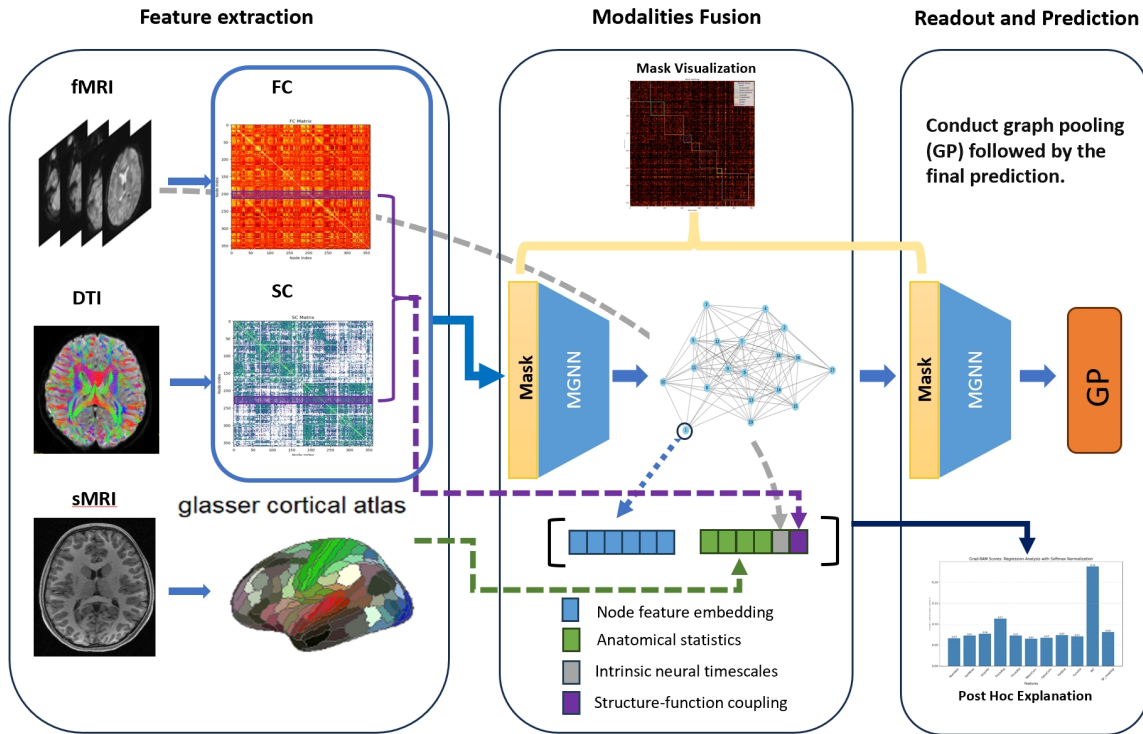


Fig. 1. Depiction of the Proposed Framework: Functional connectivity (FC) and structural connectivity (SC) obtained from fMRI and DTI, respectively, are amalgamated at the nodal level and subsequently fed into the MaskGNN for predictive analysis. In the latent space, embeddings of nodal features are integrated with anatomical statistics (AS) from sMRI, alongside a computation of structure-functional coupling using the FC and SC matrices. The aggregated features are then subjected to MaskGNN embedding, graph pooling, and readout processes. After post-training, visualization of the uniform mask across MaskGNN layers is achieved, and a posthoc approach elucidates the contribution of AS.

2. Method

2.1. Multimodal neuroimaging Integration

To mitigate the issue of heterogeneity inherent in integrating multiple neuroimaging modalities, the Glasser atlas (Glasser et al., 2016) is applied to standardize the parcellation of these modalities within a unified graph framework, employing consistent Q nodes. This approach facilitates the creation of an extensive neuroanatomical map of the human neocortex, encompassing a variety of imaging modalities, thereby advancing the coherence and comparability of neuroimaging analyses. Specifically, the Glasser atlas employs a gradient-based cortical parcellation approach, utilizing a rich array of multi-modal data, including architectural information from T1w/T2w imaging and cortical thickness maps, task-based and resting-state fMRI, connectivity patterns, and topographical organization. By integrating these diverse data sources, the atlas delineates cortical areas with exceptional precision. Besides, initial areal boundaries are identified based on co-localized gradient ridges across modalities, ensuring a robust, data-driven yet expert-validated mapping process. This semi-automated approach is further refined with machine learning classifiers trained on multi-modal feature maps to automate areal delineation and identification in individuals. Moreover, the methodology prioritizes minimal smoothing and employs multimodal surface matching (MSM) for cortical registration, focusing on areal features over folding patterns to enhance subject alignment without overfitting. Utilizing the Glasser atlas enables the

computation of FC, SC, and AS from fMRI, DTI, and sMRI data, respectively, aligning these analyses to a consistent set of ROIs. This alignment facilitates the integration and concatenation of data at the ROI level for multi-modal data fusion.

To enrich the analytical robustness of the AS features, we augment the feature vector on each ROI with structure-function coupling, employing the Spearman rank-order correlation coefficient (Baum et al., 2020) to quantitatively assess the relationship between FC and SC. Given a set of FC and SC vectors for a ROI, the Spearman rank-order correlation coefficient ρ (Chok, 2010), is shown in Eq.1.

$$\rho = 1 - \frac{6 \sum d_i^2}{n(n^2 - 1)}, \quad (1)$$

where d_i denotes the difference between the ranks of corresponding FC and SC values, and n is the total number of observations.

The calculation sequence for the Spearman rank-order correlation coefficient, ρ_i , followed by the augmentation of the AS feature sets is shown below:

1. Assign ranks to both FC and SC values.
2. Determine the rank difference, d_i , for each corresponding FC and SC pair.
3. Compute the square of each rank difference, yielding d_i^2 .
4. Aggregate these squared differences to produce $\sum d_i^2$.

This procedure is mathematically articulated as:

$$\begin{aligned} \rho_i &= \text{Spearman}(\text{FC}(i), \text{SC}(i)) \\ \text{AS}(i)' &= \text{AS}(i) \oplus \rho(i), \end{aligned} \quad (2)$$

where $\text{FC}(i)$ and $\text{SC}(i)$ denote the functional and structural connectivity vectors for the i_{th} ROI, respectively; and the symbol \oplus represents the operation of concatenation. $\rho(i)$ value close to 1 indicates a strong positive association, that is, as FC increases, SC also increases. Conversely, a value close to -1 suggests a strong negative association, where an increase in FC corresponds to the decrease in SC. A value around 0 indicates no significant correlation between FC and SC within the ROI. This approach allows for a quantitative assessment of how closely the functional interactions between brain regions (as measured by FC) correspond to their physical connections (as indicated by SC), providing insights into the structure-function relationship within each ROI.

2.2. Masked Graph Neural Networks (MaskGNN)

In our approach, we leverage edge mask learning (Qu *et al.*, 2021b) published by us to provide interpretability to our framework on an edge-based level. This methodology diverges from traditional practices where explainability is sought through patterns within individual modalities. Instead, we opt for a unified strategy, retraining our model to simultaneously acquire an edge mask matrix that encompasses subjects across various modalities. This process hinges on the consideration of only indirect graphs, necessitating the edge mask to adhere to symmetry and non-negativity. These constraints are encapsulated in the equation:

$$\mathbf{M} = \text{sigmoid}(\mathbf{V} + \mathbf{V}^T), \quad (3)$$

where \mathbf{M} serves as the mask, with each entry reflecting the important scores attributed to corresponding edges. The matrix $\mathbf{V} \in \mathbb{R}^{Q \times Q}$ represents the variable we aim to optimize with Q denoting the number of graph nodes. Through the application of the sigmoid function, we ensure that the elements within \mathbf{M} remain positive and are normalized between 0 and 1. This innovative approach not only enhances the interpretability of our framework but also ensures a holistic understanding by integrating insights across all considered modalities, thereby advancing model interpretability. Theoretically, our edge mask is applicable across all message-passing graph neural networks, as it adjusts edge weights to tailor neighborhood information aggregation. We employ the Graph Convolutional Neural Network (GCN), as shown in Eq.4, for our specific MaskGNN backbone module due to its superior performance on our dataset.

$$\mathbf{H}^{l+1} = \phi^l((\mathbf{M} + \mathbf{I}) \odot (\tilde{\mathbf{D}}^{-\frac{1}{2}} \tilde{\mathbf{A}} \tilde{\mathbf{D}}^{-\frac{1}{2}}) \mathbf{H}^l \Theta^l), \quad (4)$$

where $\tilde{\mathbf{A}} = \mathbf{A} + \mathbf{I}$ represents the augmented adjacency matrix with \mathbf{I} being the identity matrix, $\tilde{\mathbf{D}}$ denotes the degree matrix corresponding to $\tilde{\mathbf{A}}$, and \odot signifies the Hadamard product; ϕ^l , \mathbf{H}^l and Θ^l are the activation function, the feature map and the weight matrix for the l_{th} layer, respectively. Incorporating the identity matrix \mathbf{I} with the mask matrix \mathbf{M} within the GCN architecture ensures an identity mapping, crucial for preventing

the graph filter's degeneration into a null matrix when \mathbf{M} equals zero. This methodology facilitates controlled information dissemination and tailored neighborhood aggregation, predicated on the learned edge weights; therefore, it preserves the graph's structural integrity and enhances model robustness by maintaining self-connections and mitigating information loss.

The initial layer of the MaskGNN produces a graph embedding $\hat{\mathbf{H}}^1$, which is then fused with anatomical statistics (AS) $\mathbf{C} \in \mathbb{R}^{Q \times d_c}$, characterized by various morphological measurements with d_c specifying the count of features. This concatenation process occurs at the node level, with each node's feature embedding being combined with the corresponding brain region's AS to guarantee both homogeneity and dimensional compatibility. This fusion is captured by the equation $\mathbf{H}^1 = \hat{\mathbf{H}}^1 \oplus \mathbf{C}$. Following this fusion, the graph is advanced to the subsequent layer of the MaskGNN and a graph pooling (GP) operation, leading to the final predictive outcome, as shown in Eq.5.

$$\hat{\mathbf{y}} = f(\text{GP}(\text{MaskGNN}(\mathbf{H}^1))). \quad (5)$$

2.3. Objective function

To optimize model performance and mitigate oversmoothing, we implement a manifold regularization term to manage the smoothness of node embeddings, represented in Eq. 6:

$$L_{\text{manifold}} = \frac{1}{2} \sum_q \sum_{j \in N_q} \|\mathbf{h}_q - \mathbf{h}_j\|_2^2 = \text{trace}(\mathbf{H}^T \mathbf{L} \mathbf{H}), \quad (6)$$

where \mathbf{H} represents the node embeddings at the last MaskGNN layer. The manifold regularization term enforces similarity among embeddings of adjacent nodes, thereby conserving local manifold structures. It quantifies this relationship using the squared Euclidean distance between embeddings of neighboring nodes, fostering continuity and incorporating the graph Laplacian \mathbf{L} to effectively enforce this smoothness constraint throughout the graph.

In addition to imposing L_1 and L_2 constraints on the mask \mathbf{M} to promote sparsity, a stringent orthonormality condition Eq.7 is enforced. This condition mandates that all rows (and columns) of the mask \mathbf{M} be mutually orthogonal unit vectors, characterized by $\|\mathbf{M}_i\| = 1$ and $\text{mean}(\mathbf{M}_i) = 0$, thereby ensuring both symmetry and orthogonality within the matrix. Such a constraint significantly enhances the model's ability to learn independent and stable features across different samples, thereby improving generalizability and mitigating the risk of overfitting. Furthermore, the regularization term associated with orthonormality in a symmetric matrix serves to maintain the learned representations close to a set of basis-like, independent features, reinforcing the structural integrity of the model.

$$L_{\text{mask}} = \lambda_1 \|\mathbf{M}\|_1 + \lambda_2 \|\mathbf{M}\|_F^2 + \lambda_3 \|\mathbf{M} \mathbf{M}^T - \mathbf{I}_Q\|_F, \quad (7)$$

where \mathbf{I}_Q is the identity matrix with dimensions matching with those of mask \mathbf{M} , and λ_{1-3} are the regularization parameters. Thus, the loss function integral to our proposed architectural framework is articulated as follows:

$$L = L_e(\hat{\mathbf{y}}, \mathbf{y}) + \alpha L_{\text{manifold}} + L_{\text{mask}}, \quad (8)$$

where $L_e(\cdot)$ denotes the error in prediction, quantified through cross-entropy in classification scenarios or mean squared error (MSE) in regression task, and α is the regularization parameter for the manifold term.

2.4. Model Interpretation

Our framework distinguishes itself through inherent interpretability, achieved by learning masks during model optimization that incorporate multimodal fusion, thereby illuminating the significance of the graph's original connectivity. However, given that mask learning is driven by the downstream predictive task, a smaller degree of sparsity may be expected to ensure optimal predictive performance. To enhance visualization and feature clarity, we judiciously adjust a visualization threshold, as shown in Eq.9.

$$\tilde{M}_{i,j} = \begin{cases} M_{i,j} & \text{if sigmoid}(M_{i,j}) > \text{threshold,} \\ 0 & \text{otherwise.} \end{cases} \quad (9)$$

In addition to analyzing the graph's connectivity, our interest extends to identifying which anatomical statistics are most pertinent to the predictive task at hand. To achieve this, we employ gradient-based methods, specifically Gradient-weighted Regression Activation Mapping (Grad-RAM) (Qu *et al.*, 2021b) and Gradient-weighted Classification Activation Mapping (Grad-CAM) (Chattopadhyay *et al.*, 2018; Hu *et al.*, 2021), to quantify the relevance of each feature that is integrated into the graph embedding within the latent space. These methods facilitate the calculation of the importance score for each feature, providing insights into their respective contributions to the model's predictions.

$$\mathbf{G} = \frac{\partial \mathbf{y}}{\partial \mathbf{C}}, \quad (10)$$

where \mathbf{y} represents the ground truth, $\mathbf{G} \in \mathbb{R}^{Q \times C}$ denotes the gradient. Therefore, modulated by the values of AS, Grad-RAM/Grad-CAM is characterized by the interaction between the values and their associated gradients through a product operation.

$$\mathbf{a} = \frac{1}{Q} \sum_{q=1}^Q \text{ReLU}(\mathbf{G}_q \odot \mathbf{C}_q), \quad (11)$$

where $\mathbf{a} \in \mathbb{R}^C$ delineates the Grad-RAM/Grad-CAM vector pertinent to AS with the incorporation of the ReLU function to exclusively preserve those features exerting a positive influence on the ultimate prediction. Following this, normalization of the activation map is methodically executed via the Softmax function. This post hoc analysis, enhanced through the incorporation of intrinsic masked GNN layer, establishes a robust framework for the interpretation of the model. Notably, it enables the systematic identification of critical biomarkers at multiple analytical strata, particularly focusing on the connection (edge) level and the detailed level of individual (node) features for a detailed comprehension of the model's predictive dynamics.

3. Experiments

3.1. Human Connectome Project-Development Dataset

The Human Connectome Project- Development (HCP-D) (Somerville *et al.*, 2018) constitutes a groundbreaking effort dedicated to delineating the progressive maturation of the connectome within a demographically representative cohort of individuals undergoing typical development, spanning ages 5 to 21 years. This study samples a broad geographic, ethnic, and socioeconomic swath of the youth population in the United States, engaging around 1,300 healthy subjects. A focused subgroup within this cohort undergoes longitudinal observation, especially during the pubertal phase (ages 9 to 17), to rigorously document the patterns of neurodevelopmental changes occurring in this pivotal phase. To ensure consistency and comprehensive coverage, the project adopts a uniform scanning protocol across various locations, utilizing sMRI, DTI, and resting-state fMRI (rs-fMRI). This approach facilitates a comprehensive examination of the brain's structure and function from multiple perspectives. Our study focuses on brain regions excluding the subcortical area and includes subjects with valid data for at least one of three modalities, encompassing a total of 528 subjects. The subject count may vary in prediction tasks within the ablation study due to the possibility of missing modalities. The distribution of age, sex, and race is detailed in Table 1 and Figure.2, respectively.

Table 1. Subject Distribution by Sex and Race

Characteristic	Count
Total Subjects	528
Sex	
Female	290
Male	238
Race	
White	330
Black or African American	60
More than one race	86
Asian	37
Others	15

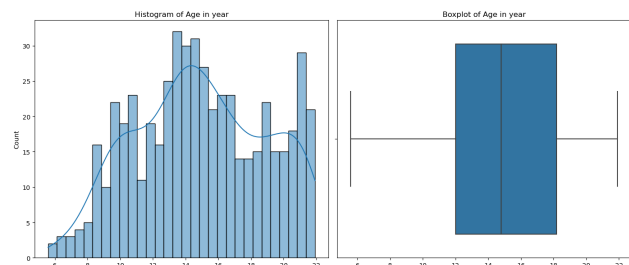


Fig. 2. The age distribution of selected subjects.

The rs-fMRI data undergo processing through the HCP minimal preprocessing pipelines (Glasser *et al.*, 2013) to address motion-related artifacts, incorporating iterative smoothing, motion parameter regression, and rigorous frame censoring (Zhang *et al.*, 2022) based on framewise displacement (FD) thresholds. For extracting resting-state functional connectivity (rs-FC) metrics, we employ 360 cortical regions of interest (ROIs) from the Glasser atlas. In parallel, DTI data are subjected to comprehensive preprocessing using MRtrix (Cruces *et al.*, 2022), including denoising, distortion and motion corrections, co-registration, multiple types of tissue extraction and streamline analysis to facilitate the calculation of SC metrics with the same ROIs. These datasets are then integrated with detailed cortical parcellation, capturing a spectrum of anatomical metrics, including

- Surface Morphology Measures:

- Number of Vertices (Kim *et al.*, 2016): Within neuroimaging, vertices denote the discrete points on the cortical surface, often derived from structural MRI data. This measure quantifies the granularity of structural analysis and is fundamental for mapping cortical morphology.
- Surface Area (Jha *et al.*, 2019; Fernández *et al.*, 2016): The surface area delineates the total extent of the cortical mantle. It serves as a crucial metric for understanding cortical expansion, folding patterns, and their implications for brain function and development.
- Gray Matter Volume (Gennatas *et al.*, 2017): Gray matter volume signifies the aggregate volume of neuronal cell bodies and dendrites within the cerebral cortex. This measure is pivotal for elucidating regional differences in neuronal density and synaptic connectivity, correlating with cognitive abilities and neuropathological conditions.

- Metrics Detailing Cortical Thickness (mean and standard deviation) (Dahnke *et al.*, 2013): Metrics detailing cortical thickness encompass measures quantifying the distance between the outer pial surface and the inner boundary surface of the cortex. These metrics facilitate the characterization of cortical architecture alterations, aiding investigations into brain aging, neurodevelopmental disorders, and neurodegenerative diseases.

- Curvature (Pienaar *et al.*, 2008):

- Mean and Gaussian Curvature: Mean curvature provides a global assessment of cortical surface curvature, while Gaussian curvature quantifies local surface curvature properties, capturing deviations from flatness in orthogonal directions. Both measures are vital for understanding cortical folding patterns and their implications for brain function and pathology.
- Intrinsic Curvature Index: The intrinsic curvature index encapsulates local variations in cortical curvature that are independent of global shape transformations.

This metric provides nuanced insights into the fine-scale cortical morphology, aiding in the characterization of cortical microstructure and its alterations in health and disease.

- Folding Index (Shimony *et al.*, 2016): The folding index delineates the degree of cortical folding, comparing observed surface area with the theoretical surface area of a smooth cortex. This metric is pivotal for identifying regions of cortical expansion or compression, shedding light on cortical morphogenesis and its aberrations in neurological disorders.
- Intrinsic Neural Timescale (Golesorkhi *et al.*, 2021; Watanabe *et al.*, 2019; Wolff *et al.*, 2022): The intrinsic neural timescale reflects the temporal dynamics of neural activity within specific cortical regions. This measure offers valuable information regarding the timescales of information processing and functional connectivity in the brain, facilitating the exploration of neural circuit dynamics and their relationship to cognitive functions.

These measures collectively offer nuanced insights into brain morphology and function in neuroimaging research which are further enhanced by incorporating structure-function coupling via the Spearman rank-order correlation coefficient, providing a detailed depiction of the brain’s anatomical and functional architecture during critical developmental stages.

To address the significant disparities in the values of SC and anatomical metrics, we employed normalization techniques. AS underwent a two-step normalization process: a logarithmic transformation to stabilize variance, followed by min-max scaling to constrain the values within a uniform range of 0 to 1. SC values were standardized by the square root of the product of gray matter volumes in the interconnected regions, as shown in Eq.12.

$$SC_{\text{normalized}}(i, j) = \frac{SC_{\text{raw}}(i, j)}{\sqrt{V_{\text{GM}}(i) \cdot V_{\text{GM}}(j)}} \quad (12)$$

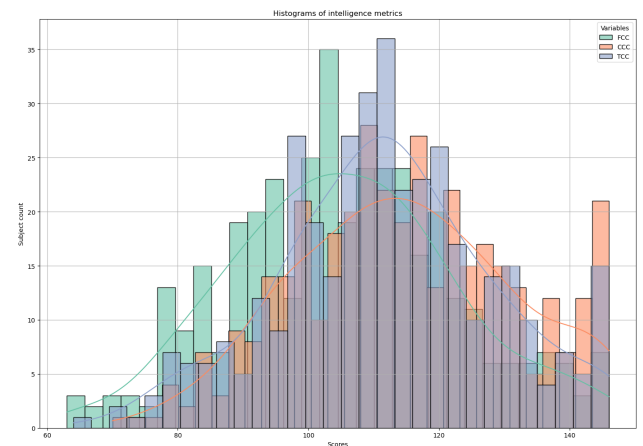
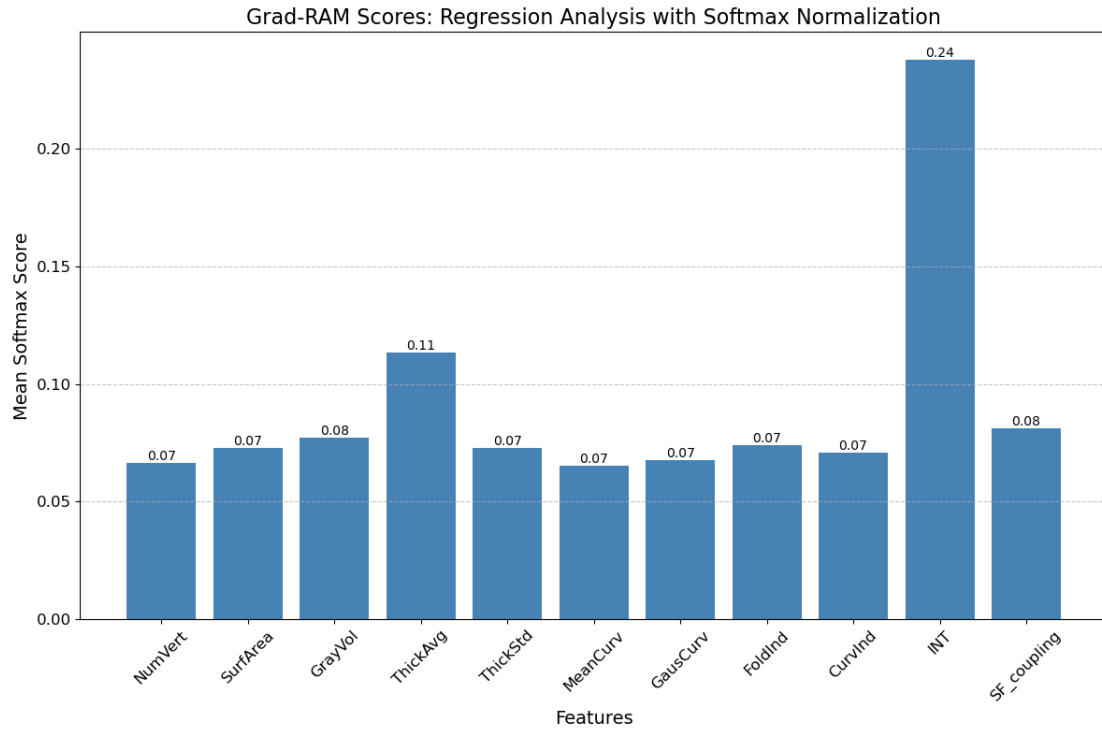
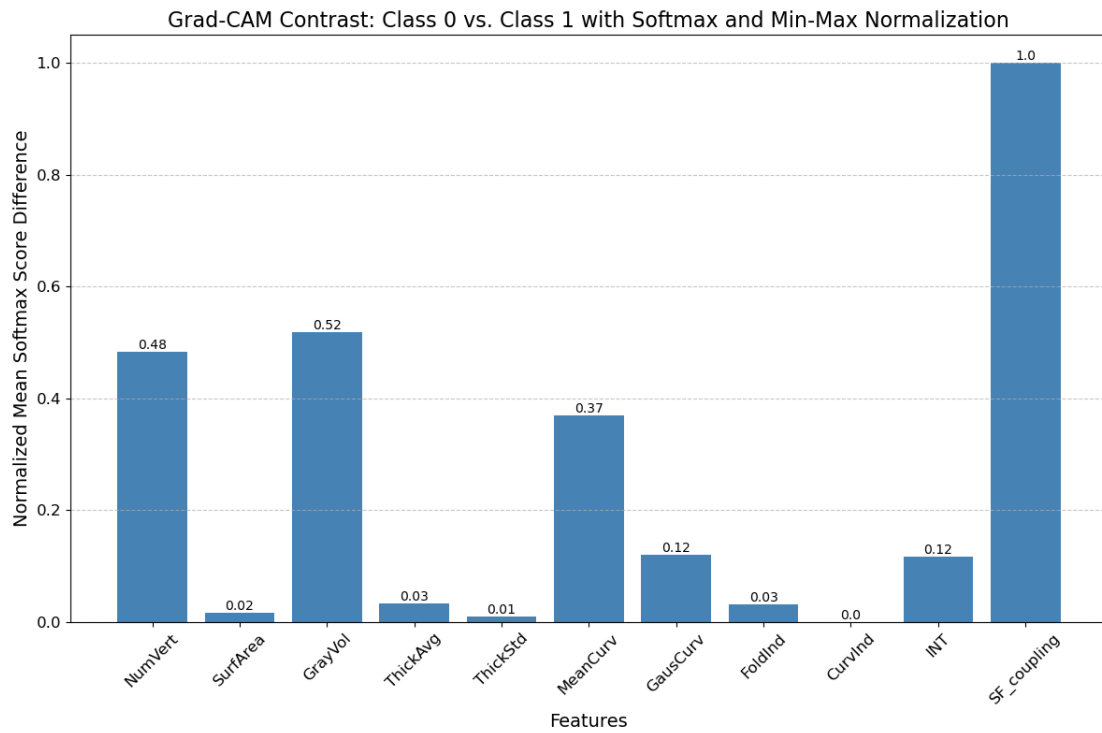


Fig. 3. The distribution of intelligence metrics.

HCP-D encompasses a range of phenotypic measurements, among which intelligence metrics such as fluid intelligence,



(a)



(b)

Fig. 4. The use of Grad-CAM and Grad-RAM scores for model explainability: (a) Grad-RAM scores for simultaneous prediction of CCC and FCC; (b) Discrimination of groups using Grad-CAM scores across distinct TCC levels

Table 2. Prediction Performance on intelligence scores.

Model	Modalities	CCC RMSE	P-value	CCC MAE	P-value	FCC RMSE	P-value	FCC MAE	P-Value
MaskGNN	FC	17.910 ± 0.118	< 0.001	14.847 ± 0.122	< 0.001	16.382 ± 0.142	< 0.001	12.973 ± 0.107	< 0.001
MaskGNN	SC	19.557 ± 0.195	< 0.001	15.305 ± 0.090	< 0.001	16.957 ± 0.021	< 0.001	13.468 ± 0.045	< 0.001
MaskGNN	FC+SC	17.580 ± 0.060	< 0.001	14.687 ± 0.059	< 0.001	16.164 ± 0.009	< 0.001	12.989 ± 0.039	< 0.001
MaskGNN	FC+SC+AS	14.968 ± 0.819	-	12.095 ± 0.534	-	14.338 ± 0.754	-	11.516 ± 0.542	-
GCN	FC+SC+AS	15.654 ± 0.127	0.026	12.366 ± 0.074	0.196	16.853 ± 0.110	< 0.001	13.727 ± 0.096	< 0.001
GAT	FC+SC+AS	16.230 ± 0.517	0.003	12.209 ± 0.099	0.574	17.531 ± 0.307	< 0.001	13.987 ± 0.190	< 0.001
GIN	FC+SC+AS	16.978 ± 1.004	< 0.001	13.768 ± 0.924	< 0.001	17.777 ± 0.712	< 0.001	14.907 ± 0.786	< 0.001
Linear	FC+SC+AS	18.061 ± 0.047	< 0.001	15.335 ± 1.776	< 0.001	17.092 ± 0.040	< 0.001	13.802 ± 1.776	< 0.001
MLP	FC+SC+AS	17.804 ± 0.576	< 0.001	14.473 ± 0.879	< 0.001	17.305 ± 0.520	< 0.001	14.430 ± 0.903	< 0.001

crystallized intelligence, and total intelligence—a composite measure of the first two—are selected as the supervisory labels for our model. Fluid intelligence is characterized by the capacity to think logically and solve new problems, independent of previously acquired knowledge. It is crucial for adapting to new situations and tackling novel challenges. In contrast, crystallized intelligence involves the application of accumulated knowledge and experience to solve problems. The model is first applied to estimate age-adjusted Crystal Cognition Composite (CCC) and age-adjusted Fluid Cognition Composite (FCC) scores using multimodal neuroimaging data for the prediction task. In the classification task, participants are next categorized into two groups based on extreme age-adjusted Total Cognition Composite Score (TCC) levels: below borderline (< 80) and very superior (> 130), highlighting significant differences. These measurements are adjusted for age variations to ensure accurate and reliable comparisons, illustrating the dynamic interplay between the capacity for innovative problem-solving and the utilization of learned knowledge. The distribution of these intelligence metrics is depicted in Figure.3.

3.2. Experimental Setup

The dataset is partitioned into training, validation, and testing subsets at the ratio of 70%, 10%, and 20%, respectively. The model undergoes training on the training set and hyperparameter tuning on the validation set. For the regression task, evaluation metrics, specifically the root mean square error (RMSE) and mean absolute error (MAE), are derived by comparing the predicted and actual test scores within the testing set. Importantly, despite variations in test scores, all participants are considered healthy, with no physical or cognitive impairments. Bootstrap analysis is employed to evaluate and benchmark the performance of models, aiming to reduce sampling bias with 10 iterations of experiments. Each deep learning model is designed with an initial two-layer structure, leading to a dense

readout layer for making predictions. Hyperparameters are optimized on a model-specific basis, employing L2 regularization and drop out to mitigate overfitting across the board. This approach is augmented by an adaptive learning rate, utilizing a ReduceLROnPlateau scheduler with a patience parameter of 10, to dynamically modify the learning rate in response to performance metrics during training and validation phases. For the MaskGNN model, the initial learning rate is established at 0.005, with training parameters set to a batch size of 32 and a maximum of 50 epochs. The L2 regularization coefficient is carefully adjusted to 1e-6 to reduce overfitting, and a sparsity parameter of 30 is used to retain only the largest K neighbor nodes in graph construction, optimizing both model complexity and computational efficiency. Hyperparameter tuning utilizes a random search approach, concentrating on variables including the initial learning rate, batch size, length of training, and the degree of regularization, etc. Moreover, the model integrates distinct regularization terms (L_1 and L_2) for mask sparsity.

3.3. Results

3.3.1. Comparative Analysis of Model Predictive Efficacy

The predictive performance of our model for intelligence metrics is compared against established benchmarks, such as Linear Regression (LR) and Multilayer Perceptron (MLP). Since our framework is general applied to other graph-based deep learning architectures, we also compare different backbone modules such as GCN, Graph Isomorphism Network (GIN), and Graph attention network (GAT), with results delineated in Table 2. From the table, the MaskGNN model emerges as the paramount model when employing a tripartite combination of modalities - FC, SC, and AS. This superiority is quantitatively supported by achieving the lowest Root Mean Square Error (RMSE) and Mean Absolute Error (MAE) across both CCC and FCC, underscored by significance tests (p-values) derived from t-tests comparing the performance of our MaskGNN

Table 3. The Performance of Group Classification Based on Intelligence Scores.

Model	Accuracy	P-value	f1-score	P-value	AUC	P-value
MaskGNN	0.870 ± 0.060	-	0.924 ± 0.035	-	0.768 ± 0.168	-
GAT	0.830 ± 0.064	0.24	0.906 ± 0.038	0.36	0.624 ± 0.056	< 0.05
GCN	0.825 ± 0.033	0.09	0.903 ± 0.020	0.18	0.519 ± 0.069	< 0.05
GIN	0.780 ± 0.046	< 0.05	0.871 ± 0.029	< 0.05	0.646 ± 0.085	0.09
MLP	0.790 ± 0.030	< 0.05	0.882 ± 0.019	< 0.05	0.543 ± 0.100	< 0.05
Linear	0.795 ± 0.027	< 0.05	0.886 ± 0.017	< 0.05	0.636 ± 0.069	< 0.05

model against competing models across repeated experiments, all below a specified threshold. Moreover, we engage in the classification task to differentiate between groups defined by high and low TCC, as illustrated in Table 3. This effort substantiates the enhanced predictive capability of our MaskGNN model, which exhibits superior accuracy and Area Under the Curve (AUC). The analysis highlights performance ranking, showing that MaskGNN outperforms both standard machine learning models and frameworks incorporating different graph-based modules, despite adopting all three multimodal strategy, while achieving lower RMSE and MAE. These findings accentuate the MaskGNN model’s capacity for nuanced intelligence score prediction through optimal multimodal data integration.

3.3.2. Ablation Study

We conduct experiments to evaluate the predictive accuracy of the MaskGNN model using solely FC, solely SC, and a combination of FC and SC without AS. The outcomes demonstrate a significant difference, as confirmed by the t-test. The ablation study on integrating modalities underscores the pivotal role of synthesizing FC, SC, and AS modalities for enhanced predictive accuracy, as shown in 2. Results demonstrate the advantages of multimodal integration that significantly boost predictive performance. The amalgamation of diverse neural data streams—FC, SC, and AS—provides a comprehensive view of the brain’s cognitive framework, thereby refining the precision of cognitive intelligence predictions.

Furthermore, we assess the influence of the manifold regularization term and the mask penalty on predictive performance by conducting a comparative analysis across four scenarios: employing solely $L_{manifold}$, solely L_{mask} , neither (establishing a baseline), and the fully proposed model. The outcomes of these comparisons are depicted in Figure.5. The analysis reveals that while both terms significantly affect performance, $L_{manifold}$ exerts a more pronounced impact due to its role in directly smoothing the embeddings.

3.3.3. Biomarker Identification

Drawing on existing knowledge, the connectivity network can be segmented into several brain functional networks: Visual, Somatomotor, Cingulo-Opercular, Dorsal-Attention, Language, Frontoparietal, Auditory, Default, and additional networks such as Posterior-Multimodal, Ventral-Multimodal, and Orbito-Affective. As illustrated in Figure.6a, the majority of these brain functional networks participate in the cognition prediction task. However, it is noteworthy that the Auditory network and language network demonstrate a marked reduction in sparsity compared to others. Moreover, the network patterns observed in our findings exhibit slight deviations from the pre-defined functional networks. This is likely a result of incorporating both SC and FC while excluding subcortical regions, which extends the network identification beyond solely functional properties. Nevertheless, discernible network patterns remain evident in our analysis. The brain connectivity patterns identified in this study are illustrated in Figure.7. This visualization provides a comprehensive overview of the neural connections discovered through our analysis, offering insights into the complex network dynamics within the brain.

Furthermore, Figure.6 reveals differences in the sparsity of masks and the chord diagrams, which illustrate the interactions between brain functional networks for classification and regression tasks, even with a consistent threshold of 0.52. Classification models, aiming to distinguish discrete groups, prioritize a selective set of discriminative connectivities, leading to sparser visual representations. In contrast, regression tasks, focusing on continuous CCC and FCC scores, incorporate a broader range of connectivities for nuanced variation capture, resulting in denser representations even with the L_1 and L_2 sparsity terms.

By applying Grad-RAM to analyze the prediction experiments, it is observed from Figure.4a that the average cortical thickness across all ROIs and the INT emerge as the top two anatomical statistics (AS) for predicting CCC and FCC scores. Meanwhile, other AS exhibit comparable Grad-RAM scores. Nonetheless, the regression task does not capture the differences among groups, where each AS may play a unique role depending on the group. Consequently, we further exam-

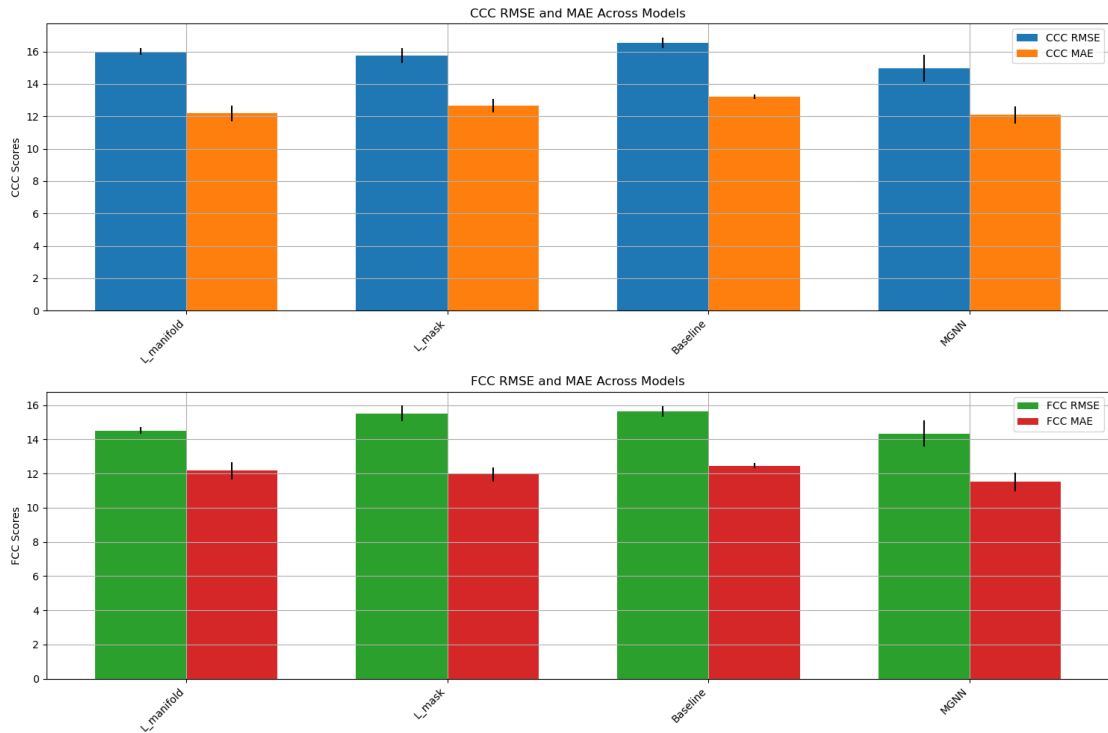


Fig. 5. A comparative analysis of predictive performance showing the individual and combined effects of the manifold regularization term ($L_{manifold}$) and mask penalty (L_{mask}) on the proposed model, with a baseline scenario for reference. All comparisons are supported by pair-wise t-tests, with p-values less than $1e - 3$ relative to the fully proposed model, highlighting significant differences.

ine the Grad-CAM scores in classifying subjects into different TCC levels, highlighting how AS influences both the extremely high and borderline TCC group. The results presented in Figure.4b reveal that the number of vertices, gray matter volume, and structure-function coupling emerge as the most distinctive features.

3.4. Discussion

3.4.1. Interactions Between Cognitive Networks and Intelligence

Our findings from Figure.6a indicate a relatively lower density in language and auditory brain functional networks in the context of predicting crystal and fluid intelligence, suggesting these networks are related yet not closely tied to the core domains of general intelligence. Given the participants' healthy status, the findings likely represent group-level variations rather than outcomes related to developmental challenges in language and academics found in individuals with hearing impairments (Heinrichs-Graham *et al.*, 2022). Supporting evidence from the study (Woolgar *et al.*, 2018) on the multiple-demand (MD) system and frontoparietal brain regions further clarifies this distinction. While the MD system's association with fluid intelligence highlights the importance of domain-general regions, the differential effects of lesions in these areas indicate a specific link between the MD system and fluid intelligence, rather than language processing alone. The distinction between nonverbal intelligence, separate from academic intelligence, and speech intelligence, linked to verbal reasoning, underscores cognitive diversity. Confirmatory factor analyses reveal auditory nonver-

bal intelligence as a distinct domain, suggesting the inclusion of a nonverbal auditory dimension in intelligence models could deepen our understanding of cognitive functions. This is supported by research showing nonverbal and speech abilities contribute uniquely to cognitive profiles, highlighting the importance of auditory processes in intelligence frameworks.

Moreover, results illustrated in Figure.6c demonstrate clear differences in Grad-CAM scores between high and low total in groups across the default mode network and cingulo-opercular network, linking cognitive abilities to distinct connectivity patterns in these networks. The association of higher-order cognitive abilities with the efficiency of the cingulo-opercular network underscores its critical role in cognitive performance. This connection is further highlighted by the impact of psychotic-like experiences (PLEs) on network efficiency and the mediation of cognitive ability by cingulo-opercular network efficiency (Sheffield *et al.*, 2016), emphasizing the cingulo-opercular network's centrality in cognitive functioning. Our analysis aligns with previous research (Hearne *et al.*, 2016; Song *et al.*, 2009; Pamplona *et al.*, 2015; Santarnecchi *et al.*, 2015) showing individual intelligence differences related to changes in resting state connectivity across networks engaged in self-referential mental activity (default mode network) and task-set maintenance (cingulo-opercular network), reinforcing the significance of connectivity variations in influencing cognitive outcomes. This relationship underscores the importance of network efficiency in cognitive health and suggests that even subtle differences in the connectivity within these networks can have substantial implications on cognitive performance.

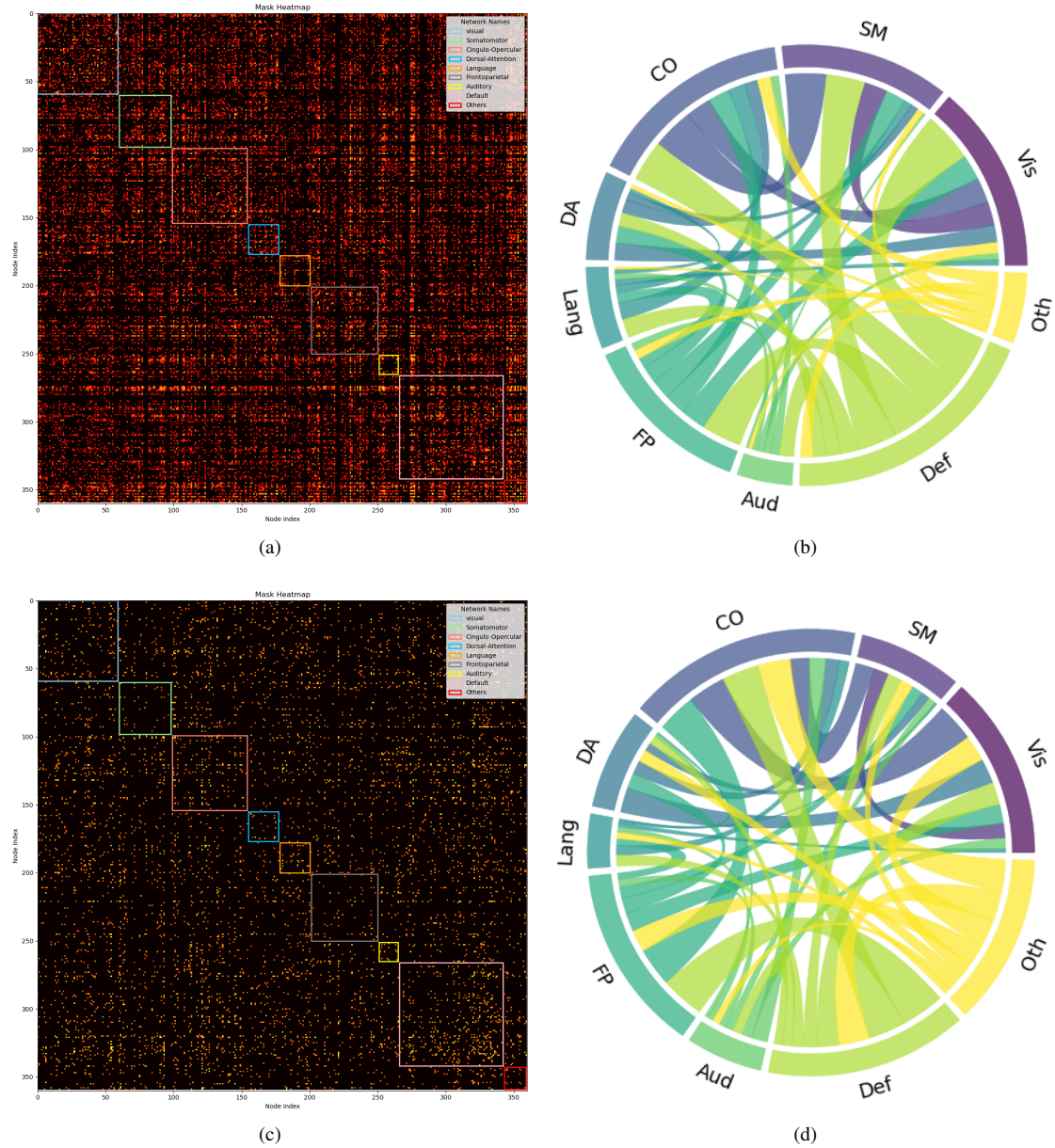


Fig. 6. The model interpretability through learned masks with 0.52 as threshold: (a) mask derived from the simultaneous prediction task for CCC and FCC; (b) Chord diagram from the simultaneous CCC and FCC prediction task, showing inter-network connections among brain functional networks, excluding intra-network links; (c) mask generated for the classification task across distinct TCC levels; (d) Chord diagram from the classification task across distinct TCC levels, showing inter-network connections among brain functional networks, excluding intra-network links. Vis-Visual, SM-Somatomotor, CO-Cingulo-Opercular, DA-Dorsal-Attention, Lang-Language, FP-Frontoparietal, Aud-Auditory, Def-Default, Oth-Others.

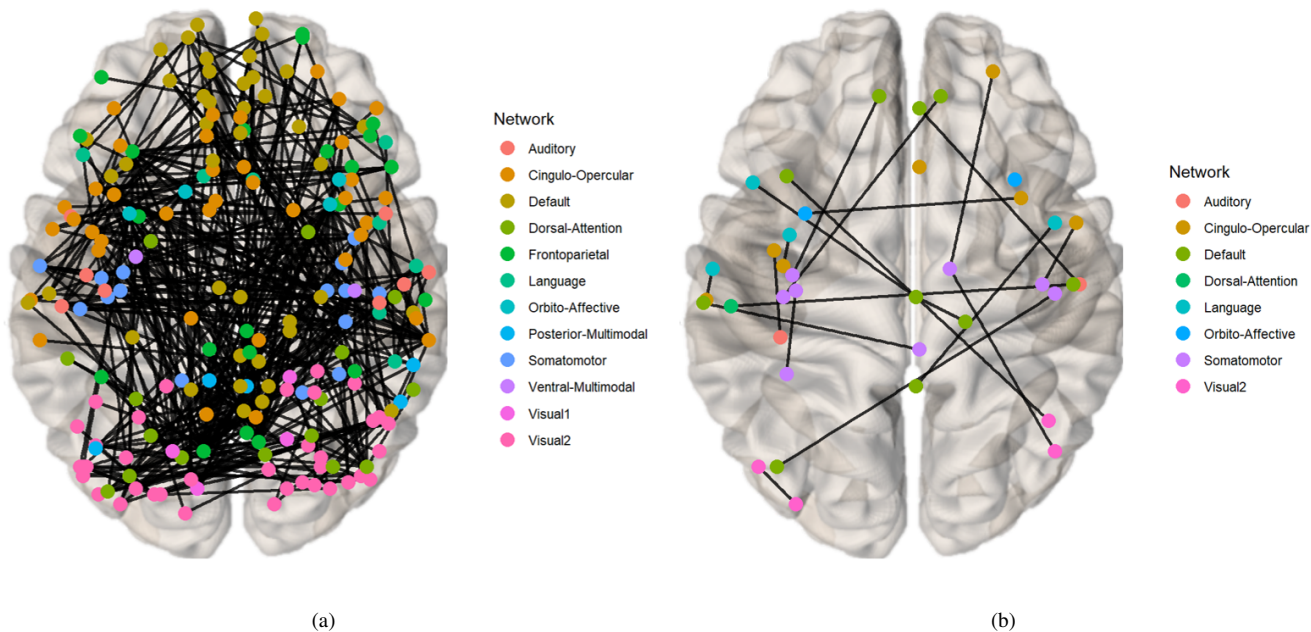


Fig. 7. The visualization of Identified Brain Connectivities: Enhanced clarity is achieved by setting the visualization threshold to 0.53. (a) Connectivity patterns identified via the mask generated from the prediction task for CCC and FCC scores. (b) Connectivity patterns identified via the mask generated from the classification task for groups with high and low TCC scores.

3.4.2. Limitations and Prospects

Regarding the proposed method, we have delineated a framework for multimodal analysis of neuroimaging data, which has been a big challenge in integrating sMRI, fMRI and DTI. Although it demonstrates high efficiency in analyzing multiple modalities of neuroimaging, the methodology employed for achieving specific outcomes warrants further refinement. Firstly, the strategy utilized for the fusion of fMRI and DTI data at the nodal level, coupled with the assimilation of the AS into the latent layer via concatenation, is preliminary. The adoption of more sophisticated fusion techniques, such as those leveraging attention mechanisms, could significantly augment the efficacy of the proposed framework. Secondly, the procedure for initializing the mask, which is a variation on our previous work, utilizes a basic approach. Alternative methodologies, such as low-rank matrix factorization, could offer improvements with the incorporation of additional prior knowledge into the analysis. In addition, we concentrate on the analysis of the HCP-D dataset, which includes only healthy individuals. Therefore, the applicability of our findings to populations with cognitive deficits or neurological disorders remains uncertain. Expanding our analysis to encompass datasets featuring subjects across a spectrum of cognitive impairments would gain additional insights and stand as an interesting direction for further study.

4. Conclusion

In this research, we introduced an integrated multimodal neuroimaging framework utilizing MaskGNN to synergize heterogeneous imaging data including fMRI, DTI, and sMRI. To our

knowledge, this work is among a handful of studies to successfully integrate fMRI, sMRI, and DTI within a novel deep learning framework. This novel approach not only harmonizes disparate data into a cohesive analytical framework but also exploits the unique strengths of each imaging modality to unravel the complexities of brain connectivity, structure and function. Our methodology, rigorously validated on the HCP-D dataset, demonstrates the importance of combining FC, SC, and AS to significantly enhance predictive accuracy in cognitive function mapping. Furthermore, by employing interpretability techniques such as learned masks and Grad-RAM/Grad-CAM analyses, we identified crucial brain connections and anatomical markers pivotal for cognitive processing. These findings affirm the efficacy of our integrated approach and provide new perspectives on the interplay between the brain's network dynamics and cognitive functionalities. Conclusively, our work offer a novel framework for the integrated examination of multimodal imaging data and for delineating the intricate relationships between the brain's structural and functional networks and their influence on cognitive development.

Data and Code availability for replication

The code is openly available at <https://github.com/GQ93>. Data cannot be open-sourced due to restrictions but can be provided upon special request.

Acknowledgments

This work was supported in part by NIH under Grants R01 GM109068, R01 MH104680, R01 MH107354,

P20 GM103472, R01 REB020407, R01 EB006841, U19AG055373, and in part by NSF under Grant #1539067.

Author contributions statement

Gang Qu was responsible for the principal data analysis, coding execution, conducting experiments, and the composition and critique of the manuscript. Aiying Zhang engaged in conceptualizing the project, data processing, and provided critical reviews of the manuscript. Ziyu Zhou and Vince D. Calhoun contributed to the evaluation of the model's design and offered valuable recommendations during the manuscript review process. Yu-Ping Wang was responsible for conceptualizing the project, securing funding, and reviewing the manuscript.

Financial Disclosures Section

All authors declare that they have no conflicts of interest.

References

- Baum, G.L., et al., 2020. Development of structure–function coupling in human brain networks during youth. *Proceedings of the National Academy of Sciences* 117, 771–778.
- Chattopadhyay, A., et al., 2018. Grad-cam++: Generalized gradient-based visual explanations for deep convolutional networks, in: 2018 IEEE winter conference on applications of computer vision (WACV), IEEE. pp. 839–847.
- Chok, N.S., 2010. Pearson's versus Spearman's and Kendall's correlation coefficients for continuous data. Ph.D. thesis. University of Pittsburgh.
- Cruces, R.R., et al., 2022. Micapipe: A pipeline for multimodal neuroimaging and connectome analysis. *NeuroImage* 263, 119612.
- Dahnke, R., et al., 2013. Cortical thickness and central surface estimation. *NeuroImage* 65, 336–348.
- Fernández, V., et al., 2016. Cerebral cortex expansion and folding: what have we learned? *The EMBO journal* 35, 1021–1044.
- Finger, H., et al., 2016. Modeling of large-scale functional brain networks based on structural connectivity from dti: comparison with eeg derived phase coupling networks and evaluation of alternative methods along the modeling path. *PLoS computational biology* 12, e1005025.
- Gennatas, E.D., et al., 2017. Age-related effects and sex differences in gray matter density, volume, mass, and cortical thickness from childhood to young adulthood. *Journal of Neuroscience* 37, 5065–5073.
- Glasser, M.F., et al., 2013. The minimal preprocessing pipelines for the human connectome project. *NeuroImage* 80, 105–124.
- Glasser, M.F., et al., 2016. A multi-modal parcellation of human cerebral cortex. *Nature* 536, 171–178.
- Glover, G.H., 2011. Overview of functional magnetic resonance imaging. *Neurosurgery Clinics* 22, 133–139.
- Golesorkhi, M., et al., 2021. The brain and its time: intrinsic neural timescales are key for input processing. *Communications biology* 4, 970.
- Hearne, L.J., et al., 2016. Functional brain networks related to individual differences in human intelligence at rest. *Scientific reports* 6, 1–8.
- Heinrichs-Graham, E., et al., 2022. Auditory experience modulates frontoparietal theta activity serving fluid intelligence. *Brain communications* 4, fcac093.
- Hofmann, S.M., et al., 2022. Towards the interpretability of deep learning models for multi-modal neuroimaging: Finding structural changes of the ageing brain. *NeuroImage* 261, 119504.
- Hu, W., et al., 2021. Interpretable multimodal fusion networks reveal mechanisms of brain cognition. *IEEE transactions on medical imaging* 40, 1474–1483.
- Jha, S.C., et al., 2019. Environmental influences on infant cortical thickness and surface area. *Cerebral Cortex* 29, 1139–1149.
- Kim, S.H., et al., 2016. Development of cortical shape in the human brain from 6 to 24 months of age via a novel measure of shape complexity. *NeuroImage* 135, 163–176.
- Li, X., et al., 2021. Braingnn: Interpretable brain graph neural network for fmri analysis. *Medical Image Analysis* 74, 102233.
- Orlichenko, A., et al., 2022a. Latent similarity identifies important functional connections for phenotype prediction. *IEEE Transactions on Biomedical Engineering*.
- Orlichenko, A., et al., 2022b. Phenotype guided interpretable graph convolutional network analysis of fmri data reveals changing brain connectivity during adolescence, in: *Medical Imaging 2022: Biomedical Applications in Molecular, Structural, and Functional Imaging*, SPIE. pp. 294–303.
- O'Donnell, L.J., Westin, C.F., 2011. An introduction to diffusion tensor image analysis. *Neurosurgery Clinics* 22, 185–196.
- Pamplona, G.S., et al., 2015. Analyzing the association between functional connectivity of the brain and intellectual performance. *Frontiers in human neuroscience* 9, 61.
- Patel, B., et al., 2024. Explainable multimodal graph isomorphism network for interpreting sex differences in adolescent neurodevelopment. *Applied Sciences* 14, 4144.
- Pienaar, R., et al., 2008. A methodology for analyzing curvature in the developing brain from preterm to adult. *International journal of imaging systems and technology* 18, 42–68.
- Qu, G., et al., 2020. A graph deep learning model for the classification of groups with different iq using resting state fmri, in: *Medical imaging 2020: Biomedical applications in molecular, structural, and functional imaging*, SPIE. pp. 52–57.
- Qu, G., et al., 2021a. Brain functional connectivity analysis via graphical deep learning. *IEEE Transactions on Biomedical Engineering* 69, 1696–1706.
- Qu, G., et al., 2021b. Ensemble manifold regularized multi-modal graph convolutional network for cognitive ability prediction. *IEEE Transactions on Biomedical Engineering* 68, 3564–3573.
- Rykhlevskaia, E., et al., 2008. Combining structural and functional neuroimaging data for studying brain connectivity: a review. *Psychophysiology* 45, 173–187.
- Santarnecchi, E., et al., 2015. Intelligence-related differences in the asymmetry of spontaneous cerebral activity. *Human brain mapping* 36, 3586–3602.
- Sheffield, J.M., et al., 2016. Cingulo-opercular network efficiency mediates the association between psychotic-like experiences and cognitive ability in the general population. *Biological psychiatry: cognitive neuroscience and neuroimaging* 1, 498–506.
- Shi, X., et al., 2020. Graph temporal ensembling based semi-supervised convolutional neural network with noisy labels for histopathology image analysis. *Medical image analysis* 60, 101624.
- Shimony, J.S., et al., 2016. Comparison of cortical folding measures for evaluation of developing human brain. *NeuroImage* 125, 780–790.
- Somerville, L.H., et al., 2018. The lifespan human connectome project in development: A large-scale study of brain connectivity development in 5–21 year olds. *NeuroImage* 183, 456–468.
- Song, M., et al., 2009. Default network and intelligence difference. *IEEE Transactions on autonomous mental development* 1, 101–109.
- Stämpfli, P., et al., 2008. Combining fmri and dti: a framework for exploring the limits of fmri-guided dti fiber tracking and for verifying dti-based fiber tractography results. *NeuroImage* 39, 119–126.
- Sui, J., et al., 2011. Discriminating schizophrenia and bipolar disorder by fusing fmri and dti in a multimodal cca+ joint ica model. *NeuroImage* 57, 839–855.
- Sui, J., et al., 2013. Three-way (n-way) fusion of brain imaging data based on mcca+ jica and its application to discriminating schizophrenia. *NeuroImage* 66, 119–132.
- Sui, J., et al., 2014. Function–structure associations of the brain: evidence from multimodal connectivity and covariance studies. *NeuroImage* 102, 11–23.
- Symms, M., et al., 2004. A review of structural magnetic resonance neuroimaging. *Journal of Neurology, Neurosurgery & Psychiatry* 75, 1235–1244.
- Tang, H., et al., 2023. Signed graph representation learning for functional-to-structural brain network mapping. *Medical image analysis* 83, 102674.
- Tang, H., et al., 2024. Ex-vivo hippocampus segmentation using diffusion-weighted mri. *Mathematics* 12, 940.
- Uludağ, K., Roebroeck, A., 2014. General overview on the merits of multimodal neuroimaging data fusion. *NeuroImage* 102, 3–10.
- Wang, J., et al., 2021. Functional network estimation using multigraph learning with application to brain maturation study. *Human brain mapping* 42, 2880–2892.
- Wang, J., et al., 2023. Dynamic weighted hypergraph convolutional network for brain functional connectome analysis. *Medical Image Analysis* 87, 102828.
- Wang, W., et al., 2024. Multiview hyperedge-aware hypergraph embedding

- learning for multisite, multiatlas fmri based functional connectivity network analysis. *Medical Image Analysis* , 103144.
- Watanabe, T., et al., 2019. Atypical intrinsic neural timescale in autism. *Elife* 8, e42256.
- Wolff, A., et al., 2022. Intrinsic neural timescales: temporal integration and segregation. *Trends in cognitive sciences* 26, 159–173.
- Woolgar, A., et al., 2018. The multiple-demand system but not the language system supports fluid intelligence. *Nature human behaviour* 2, 200.
- Xiao, L., et al., 2022. Distance correlation-based brain functional connectivity estimation and non-convex multi-task learning for developmental fmri studies. *IEEE Transactions on Biomedical Engineering* 69, 3039–3050.
- Yan, W., et al., 2022. Deep learning in neuroimaging: Promises and challenges. *IEEE Signal Processing Magazine* 39, 87–98.
- Zhang, A., et al., 2022. Decoding age-specific changes in brain functional connectivity using a sliding-window based clustering method. *bioRxiv* , 2022–09.
- Zhou, Z., et al., 2024. An interpretable cross-attentive multi-modal mri fusion framework for schizophrenia diagnosis. *arXiv preprint arXiv:2404.00144* .
- Zhu, D., et al., 2014. Fusing dti and fmri data: a survey of methods and applications. *NeuroImage* 102, 184–191.
- Zhu, Q., et al., 2022. Multimodal triplet attention network for brain disease diagnosis. *IEEE Transactions on Medical Imaging* 41, 3884–3894.
- Zhuang, H., et al., 2019. Multimodal classification of drug-naïve first-episode schizophrenia combining anatomical, diffusion and resting state functional resonance imaging. *Neuroscience letters* 705, 87–93.